

Superresolution Imaging of Dynamic MreB Filaments in *B. subtilis*—A Multiple-Motor-Driven Transport?

Philipp v. Olshausen,^{††} Hervé Joël Defeu Soufo,[§] Kai Wicker,^{¶||††} Rainer Heintzmann,^{¶||††}
Peter L. Graumann,^{§††§§} and Alexander Rohrbach^{††*}

[†]Laboratory for Bio- and Nano-Photonics, Department of Microsystems Engineering-IMTEK, [‡]BIOS Centre for Biological Signalling Studies, and [§]Department of Microbiology, Faculty of Biology, University of Freiburg, Freiburg, Germany; [¶]Institute of Physical Chemistry, Abbe Center of Photonics, Friedrich Schiller University Jena, Jena, Germany; ^{||}Institute of Photonic Technology, Jena, Germany; ^{††}King's College London, Randall Division, London, UK; ^{‡‡}SYNMIKRO, LOEWE Centre for Synthetic Microbiology, and ^{§§}Faculty of Chemistry, University of Marburg, Marburg, Germany

ABSTRACT The cytoskeletal protein MreB is an essential component of the bacterial cell-shape generation system. Using a superresolution variant of total internal reflection microscopy with structured illumination, as well as three-dimensional stacks of deconvolved epifluorescence microscopy, we found that inside living *Bacillus subtilis* cells, MreB forms filamentous structures of variable lengths, typically not longer than 1 μm . These filaments move along their orientation and mainly perpendicular to the long bacterial axis, revealing a maximal velocity at an intermediate length and a decreasing velocity with increasing filament length. Filaments move along straight trajectories but can reverse or alter their direction of propagation. Based on our measurements, we provide a mechanistic model that is consistent with all observations. In this model, MreB filaments mechanically couple several motors that putatively synthesize the cell wall, whereas the filaments' traces mirror the trajectories of the motors. On the basis of our mechanistic model, we developed a mathematical model that can explain the nonlinear velocity length dependence. We deduce that the coupling of cell wall synthesis motors determines the MreB filament transport velocity, and the filament mechanically controls a concerted synthesis of parallel peptidoglycan strands to improve cell wall stability.

INTRODUCTION

Living cells use a common set of molecular mechanisms to carry out their basic functions owing to their evolution from common ancestors. This is the first article of faith of the reductionist approach (1) and connects general principles known from eukaryotic cells to similar principles ruling in bacteria. One of these principles is the interplay between the cytoskeleton and molecular machines, such as myosin motor proteins, that perform mechanical work along actin filaments. The proteins MreB and ParM not only have ancestors in common with actin, but also reveal a structure very similar to that of actin (2). Like actin, MreB and ParM form magnesium- and ATP- (or GTP-) dependent filaments in vitro. In contrast to actin, MreB can form straight double filaments, sheets of filaments, or helical MreB filaments (2–4). MreB localizes underneath the bacterial cell membrane (CM) in many rod-shaped bacteria, such as *Escherichia coli*, *Bacillus subtilis*, and *Caulobacter crescentus*, and is an essential protein in many species (5). The depletion of MreB or the dissipation of MreB structures through a small-molecule inhibitor lead to a loss of rod shape until the cells become round and lyse. Also, a point mutation in the ATP binding pocket has an effect on cell morphology (6,7). Additionally, MreB affects the positioning of intracellular protein complexes and even cell-surface structures in many bacterial species (8–12).

Although some details about the structures and binding affinities of the cytoskeletal elements MreB, transmembrane proteins (TMPs) such as MreC, MreD, RodA, and RodZ, and the processive cell wall (CW) synthesis machinery, including different penicillin-binding proteins (PBPs), are known, the role of the cytoskeletal protein MreB in cellular organization remains mysterious. In other words, the second article of faith in reductionism—understanding the function that results from the molecules assembling to filaments—has not yet been achieved.

Regarding the function of MreB in conjunction with peptidoglycan (PG) strands in the CW, it has been found that MreB helps to pattern the CW (13,14) but also contributes to the mechanical stability in *E. coli* (15). However, using total internal reflection fluorescence microscopy (TIRF-M), various investigators have come to the conclusion that MreB does not form filaments, but rather patch-like or point-like structures that passively move along with the PG strand extension machinery (acting as molecular motor) in a circumferential motion with stochastic direction reversals (16–18). These ideas would make a contribution to the cell's mechanical stability difficult to imagine, and they would suggest that the fundamental aspect of the formation of extended filamentous structures, which affects cell shape and other dynamic subcellular processes, differs between MreB and actin, and that the function of MreB does not rely on its ability to form extended filaments (19).

Available information about the structure and dynamics of the cytoskeleton, especially in bacteria, is incomplete

Submitted January 24, 2013, and accepted for publication July 26, 2013.

*Correspondence: rohrbach@imtek.de

Editor: David Odde.

© 2013 by the Biophysical Society
0006-3495/13/09/1171/11 \$2.00



because of the limited optical resolution in light microscopy and a lack of specific labels for the cytoskeleton in electron microscopy. However, during the last few years, a variety of optical superresolution microscopy techniques based on fluorescence staining, such as stimulated emission depletion (STED) (20) and photo-activated localization microscopy (PALM)/stochastic optical reconstruction microscopy (STORM) (21–23), have emerged. In this study, we present a combination of TIRF-M and structured illumination microscopy (SIM) (24) that provides enhanced contrast due to a reduction of the background fluorescence (TIRF) and an increase in spatial resolution of 200–240% relative to conventional fluorescence microscopy. This allows us to resolve object structures with a resolution of ~120 nm inside living cells at a frame rate of nearly 1 Hz.

This fast, high-contrast superresolution imaging technique allows us to investigate the structure and dynamics of MreB and its possible functionality. In addition to the question as to whether MreB forms filament-like structures or more patch-like structures, we address the fundamental aspects of the motion of MreB structures (25), which have been postulated to be driven by the CW synthesis motors (16–18). Based simply on the observed phenomena of bidirectional transport of MreB and a filament length-dependent velocity, we derive a multiple-motor model for the spatial organization between MreB filaments and PG strands. This model is tested conceptually for all observed dynamics of MreB. Additionally, a simplified mathematical model is provided that quantitatively accounts for the length-dependent velocity, representing the third article of faith in the reductionist approach.

MATERIALS AND METHODS

TIRF-SIM

The TIRF-SIM technique in combination with a computer holographic illumination control (24,26) was implemented on an in-house-made microscopy system. As indicated in Fig. 1 F, three pairs of counterpropagating evanescent waves (EWs) with angles of 60° to each other are generated by a computer hologram (spatial light modulator (SLM)) to form images with a sinusoidal structured illumination (grids 1–3). In total, 3×3 partial images are taken for each superresolved image. Therefore, each grid is shifted twice over one grid period to illuminate every point of the object equally. The final image is reconstructed from all partial images using a custom MATLAB-based algorithm (The MathWorks, Natick, MA; for details, see Supporting Material, text 1a).

Image acquisition

Living *B. subtilis* cells were pipetted on a No. 1.5 coverslip and covered with a 2% agarose pad of PBS buffer. All images were acquired within 90 min after mounting of the sample. The majority of the time-lapse data were acquired at 5 s intervals. Some faster sequences with time steps of 2.2 s were also acquired. Before each image acquisition, an automatic refocusing was performed.

For a detailed description of the data analysis and the growth conditions for the bacterial strains, see Supporting Material, text 1.

RESULTS

2D superresolution imaging

In superresolution fluorescence microscopy, significantly more excitation light and also more fluorescence photons are needed compared with conventional microscopy. Therefore, these techniques are more subject to photobleaching than conventional microscopy, and accordingly, the total number of images that can be acquired over the total measurement time is limited. Consequently, the acquisition of a representative two-dimensional (2D) image allows longer time series than the acquisition of a three-dimensional (3D) superresolved image stack per time point. In this context, TIRF-M is particularly useful because only one section of the object is illuminated and detected, whereas in confocal microscopy the whole object is illuminated for each section. Besides providing minimal bleaching, TIRF-M can be well combined with SIM, where two counterpropagating EWs emerging from TIR form a standing wave. The EWs are coupled to the glass coverslip and their interference results in a fine illumination grid that illuminates or darkens fine structures in the object (Fig. 1 F). Using TIRF-SIM, we can achieve a 2.4-fold increase in spatial resolution relative to conventional TIRF-M. This results in a 120 nm resolution inside living cells (Fig. S1) at a maximal frame rate of 0.8 Hz. Integration times per partial image are 35–60 ms.

As shown in Fig. 1 F, illumination by conventional TIRF using a single EW (indicated by a blue single focused beam FB_0 in the back focal plane (BFP)) results in a fluorescence image of GFP-labeled MreB structures inside *B. subtilis*, which is overlaid by a conventional bright-field (CBF) image in Fig. 1 E. Although in the TIRF image both the contrast and the lateral resolution of ~240 nm are good (Fig. 1 A), a significant improvement in spatial resolution is achieved by TIRF-SIM, as revealed by Fig. 1, B and D. A fourth imaging mode was applied to obtain an overall impression of the MreB distribution: a 3D image stack using epifluorescence (3D-epi) was acquired, slice-wise combined, and 3D deconvolved (using Autodeblur; Media Cybernetics), resulting in the volume-rendered representation plotted in Fig. 1 C.

MreB forms filaments of variable lengths

As already indicated by the TIRF images of MreB polymers in *B. subtilis*, the TIRF-SIM images in Fig. 1, B and D, clearly reveal that MreB forms filaments of variable lengths inside *B. subtilis* when they are in the phase of exponential growth. Because the fluorescent MreB fusion protein was expressed from exogenous xylose promoter (*pxyl-gfp-mreB*), we ruled out the influence of a possible overexpression on filament length in two ways: First, we performed a western blot analysis showing no overexpression of GFP-MreB compared with wild-type MreB (Fig. S2). Second,

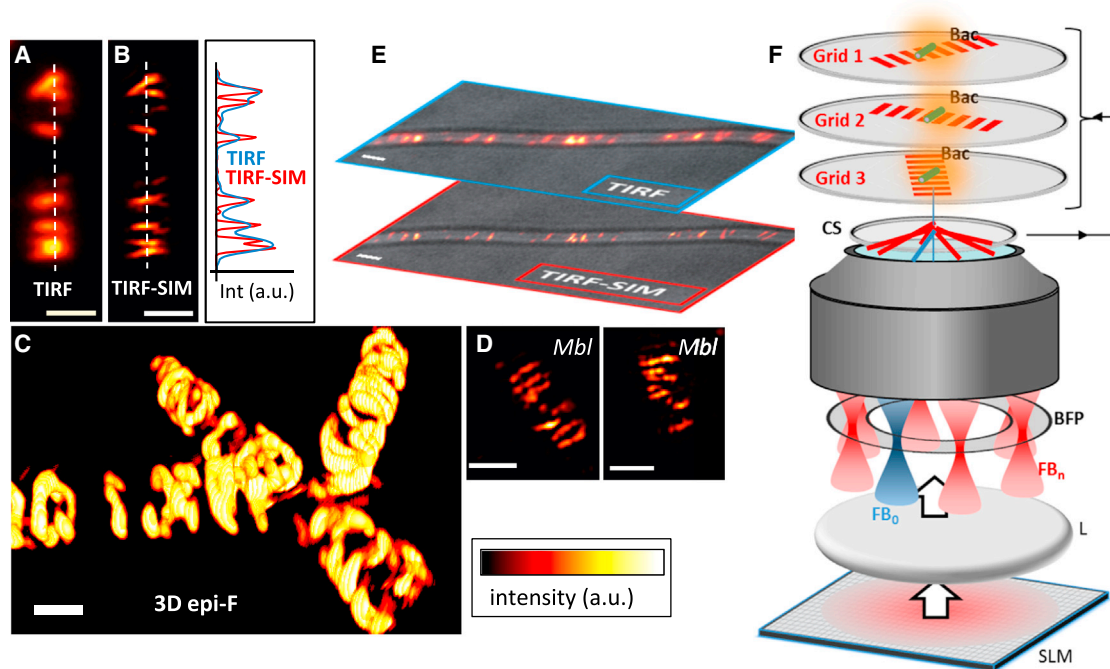


FIGURE 1 Fluorescence microscopy scheme and images of MreB/Mbl in *B. subtilis*. (A) TIRF image of GFP-MreB in a single *B. subtilis* cell. (B) Superresolved TIRF-SIM image of the same cell. The filamentous structure of MreB becomes clearly visible. The two intensity profiles along the dashed lines demonstrate the increase in resolution. (C) Volume rendering of a deconvolved 3D epifluorescence stack. MreB is located only at the outskirts of the rod-shaped cells. The 1 μm scale bar serves as a length estimate. (D) TIRF-SIM images of GFP-Mbl filaments expressed from its original promoter. (E) Overlay image from normal TIRF, superresolved TIRF-SIM, and bright-field illumination. (F) Phase holograms displayed on an SLM are used to generate different point-like illumination orders in the BFP of the objective lens. For TIRF conditions, one focused beam (FB_0 , blue) is positioned in the TIR region. For TIRF-SIM pairs of opposing foci (FB_n , $n = 1,2,3$) are placed in the TIR region of the BFP, resulting in sinusoidal illumination grids of different orientations (grids 1–3) at the coverslip (CS)-sample interface. Scale bars are 1 μm .

we expressed a second *B. subtilis* actin-like protein, Mbl, fused to GFP (GFP-Mbl) as the sole source of the protein using its original promoter (*pmb1-gfp-mbl*). We found very similar lengths of GFP-Mbl compared with those of the MreB filaments, as shown in Fig. 1 D. By analyzing the deconvolved 3D image stacks, we measured lengths between $L_{\text{min}} \approx 0.1 \mu\text{m}$ up to half a circumference ($L_{\text{max}} = 1.5 \mu\text{m}$), assuming a typical circumference of $C = \pi \times D \approx 3 \mu\text{m}$ for bacteria with a mean diameter of $D = 1 \mu\text{m}$. The results are similar for Mbl (with original promoter) with a mean length $\langle L \rangle = 0.44 \mu\text{m} \pm 0.32 \mu\text{m}$ ($N = 39$) and MreB (expressed from original locus) with $\langle L \rangle = 0.62 \mu\text{m} \pm 0.47 \mu\text{m}$ ($N = 87$). The histograms of the corresponding length distributions are shown in Fig. S3.

Transport of MreB filaments

We now address the question as to whether MreB is moved passively by treadmilling, which is a well-known mechanism especially for actin filaments to control cell migration or growth cone dynamics. Treadmilling requires a net depolymerization rate $-(r_{\text{on}}^- \cdot c_{\text{TM}} - r_{\text{off}}^-)$ at one filament end (minus end) similar to the net polymerization rate $r_{\text{on}}^+ \cdot c_{\text{TM}} - r_{\text{off}}^+$ at the other end (plus end), where the on-rates

$r_{\text{on}}^{+/-}$ are concentration dependent. This leads to a passive self-transport of the filament if both net rates are approximately equal. This situation depends sensitively on the concentration of free monomers in the cytosol, which must be $c_{\text{TM}} = (r_{\text{off}}^+ + r_{\text{off}}^-)/(r_{\text{on}}^+ + r_{\text{on}}^-)$ in the case of treadmilling (TM). In this case, MreB monomers inside the filaments would not move relative to fixed points in the CW.

The other concept used by nature for a directed transport is force generation by molecular motors. Also well established for actin, various types of myosin motors either transport cargos along filaments (processive motors) or displace actin filaments as, e.g., in muscles (nonprocessive motors). The resulting transport forces and velocities depend on the cooperativity of the motors, which is often characterized by the duty ratio $R = \tau_{\text{on}}/(\tau_{\text{on}} + \tau_{\text{off}})$, i.e., the time τ_{on} a motor is bound as a fraction of the total time of observation $\tau_{\text{tot}} = (\tau_{\text{on}} + \tau_{\text{off}})$. In *B. subtilis*, these motors must be located near the CM and could be connected to the CW synthesis machinery by several TMPs and PBPs (16–18). Remarkably, PBPs were shown to on-bind and off-bind from the membrane complexes with as yet unknown times τ_{on} and τ_{off} (16).

As previously proposed by other authors, we predicate that MreB filaments do not move due to treadmilling,

but by a transport through molecular synthesis motors (16–18). This claim is corroborated by a number of single-filament events that we analyzed in their directional dynamics, as shown in time sequences in Fig. 2. These time series of a small population of bacteria typically consist of 30–40

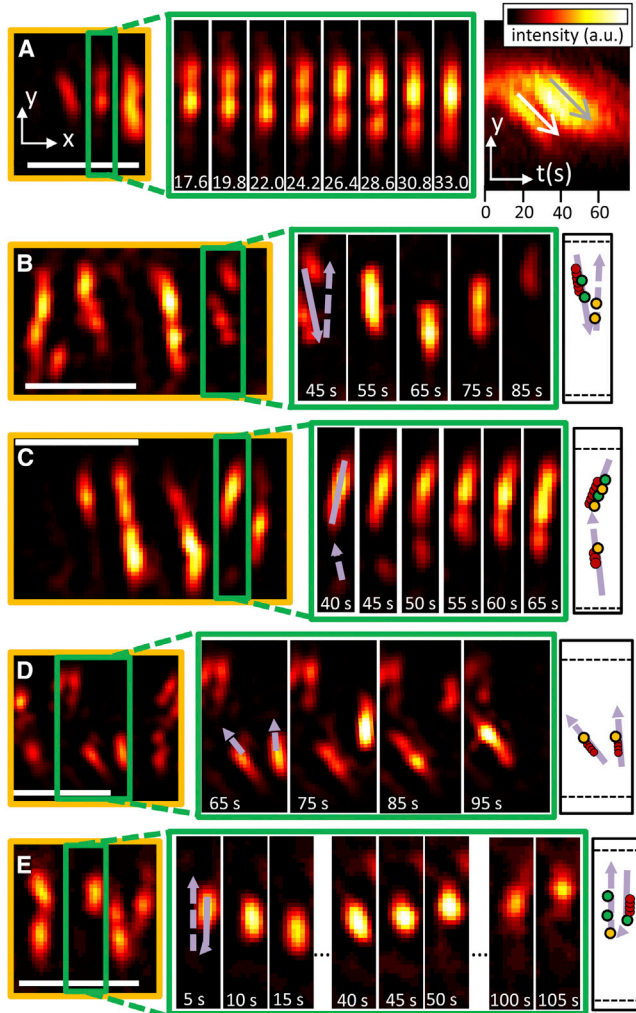


FIGURE 2 Single-filament events observed by TIRF-SIM. On the left, parts of cells are shown. Image sequences of several time points of the areas framed by a green box are displayed on the right. Additionally, either a kymograph or a scheme of the proposed motor model corresponding to the shown event is given. P- and/or m-motors (green and orange, respectively) are coupled by MreB filaments (red) and run along straight tracks (light purple). (A) A filament enters the TIRF region and exhibits an intensity substructure that moves synchronously with the leading edge over many time points, which can also be well observed in the kymograph to the right. This cannot be explained by treadmilling. (B) A filament reverses its direction of transport concomitantly with a slight change of orientation. Scheme: Opposing motors win a tug-of-war and take over the MreB filament, transporting it along a slightly tilted track. (C) A short filament is stopped in its movement by an opposing, static one. (D) Two neighboring filaments are transported at an angle of $\sim 35^\circ$ to each other. (E) A short filament undergoes several tug-of-wars during the observed time window. It moves down, stops for ~ 30 s, reverses for a short distance, stops again for ~ 50 s, and finally continues and disappears. Scale bar is $1 \mu\text{m}$.

images with time steps of 2–5 s such that $\tau_{tot} \approx 1\text{--}3$ min. Typical time-lapse videos recorded with TIRF-SIM are available as Movie S1. Fig. 2 A, left, displays a $1 \mu\text{m}^2$ large image area showing fluorescent MreB filaments from a living bacterium. A region of interest (ROI) is highlighted by a green frame that illustrates the movement of a filament entering the TIRF region over 17 s, depicted by eight time points. The filament reveals an intensity structure along its axis due to an irregular density of fluorophores or MreB monomers. Remarkably, the intensity structure is transported downward synchronously with the leading edge over many time points, which is further illustrated by the kymograph on the right side of Fig. 2 A. This example indicates that the filament is transported as a whole, which is made possible by motors near the CM pulling or pushing the filament, but not by treadmilling. Another ROI depicted in Fig. 2 B illustrates the spontaneous reversal of filament propagation within <10 s over a total recording time of 40 s. Here, two points are striking after a reversal in direction: first, the filament's leading and trailing edges are exchanged, and second, the filament moves along a different trajectory—an event we observed frequently. A trajectory is defined by the time projection of a filament image before or after a reversal and always results in straight lines. A reversal in direction due to treadmilling would require a sudden change in the (de-)polymerization rates such that c_{TM} would remain approximately constant. This seems to be a rather unlikely situation, although several factors may regulate the MreB polymerization rate (3,27). Furthermore, the corresponding orientational change of the trajectory cannot be explained by treadmilling either. Fig. 2 C documents the movement of a short filament, which is stopped by an opposing, static filament. Fig. 2 D shows how two neighboring filaments are transported at an angle of $\sim 35^\circ$ to each other. The single-filament event in Fig. 2 E illustrates a noncontinuous transport with both stop-and-go and reversal of direction during the observed time window of 105 s. This behavior can be well explained by a mechanistic model in which multiple motors acting in both directions are attached to MreB filaments, as discussed further below.

MreB trajectories and transport tracks

Besides the reversal in direction, we also ascertain that the trajectories of MreB can have large angles relative to each other, as indicated in Fig. 2 D. The change in the filament propagation angle and in trajectory also in the forward direction is further manifested by the ROI in Fig. 2 B. MreB moves along straight trajectories, which probably trace the PG synthesis tracks that are connected to MreB. Although they are already visible in Figs. 1 B and 2 D, the traces occur over a broad range of angles. Maximum deflections $\Delta\theta \approx \pm 30^\circ$ around the mean angle $\langle\theta\rangle = 90^\circ$ to the bacterial long axis are revealed in histograms

in Fig. S4. The best way to visualize traces or the putative tracks is to use time projections of a time series of moving filaments. This is demonstrated in Fig. 3, where the angular distribution of filaments at the bottom of the bacterium is visible together with another remarkable effect: after examining hundreds of filament traces (see Fig. S5), we detect that traces never cross each other. Also, some traces seem to be constrained by others, which suggests that one moving filament can be stopped by another filament (see also Fig. 2 C and Movie S2). A connection between MreB and the PG strands is assumed, however, it is subject of our discussion whether the traces of MreB filament dynamics mirror the distribution of PG strands in the CW.

Transport velocities

We assessed the filament velocities from TIRF-SIM time-lapse images by analyzing the fluorescence kymographs $F(s,t)$ of single filaments propagating in direction s ($N \approx 105$ for MreB, $N \approx 30$ for Mbl). The velocities v_F of the filament edges along the filament axis in direction s were obtained by linear fitting the edges as indicated in Fig. 4 A. v_F was determined by only one edge of each filament, which is justified by the constant filament length as outlined in Fig. 4 A by the vertical widths (blue bars). For both the MreB and Mbl filaments, we found mean velocities of $\langle |v_F| \rangle \approx 19$ nm/s, which we found to be direction independent for MreB, although the MreB filaments have a broader velocity distribution than the Mbl filaments (Fig. S6). The mean velocity corresponds to roughly half a cell circumference C per minute, $\langle |v_F| \rangle \approx 1/2 C/\text{min}$. The distribution of velocities v_F is strongly dependent on filament length L . As displayed in Fig. 4 A, the length L is obtained by the width of the fluorescence distribution in $F(s,t)$. The observation time was $\tau_{mes} = 88\text{--}150$ s over 30–40 frames. Although the observation is spatially limited by the evanescent illumination to the bottom of the bacterium, it is easily visible that shorter filaments move faster than longer ones (see Movie S1). However, the quantitative single-filament analysis reveals that for short filament

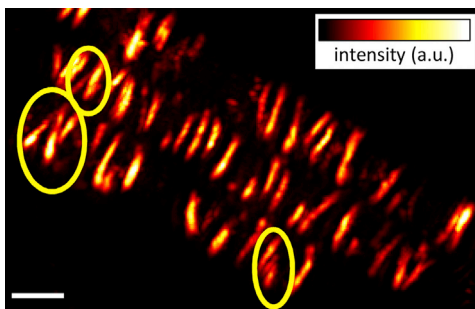


FIGURE 3 Time projection of an image sequence of MreB filaments reflects MreB traces. The traces never cross each other. Three yellow circles indicate where one trace is constrained by another. Scale bar is 1 μm .

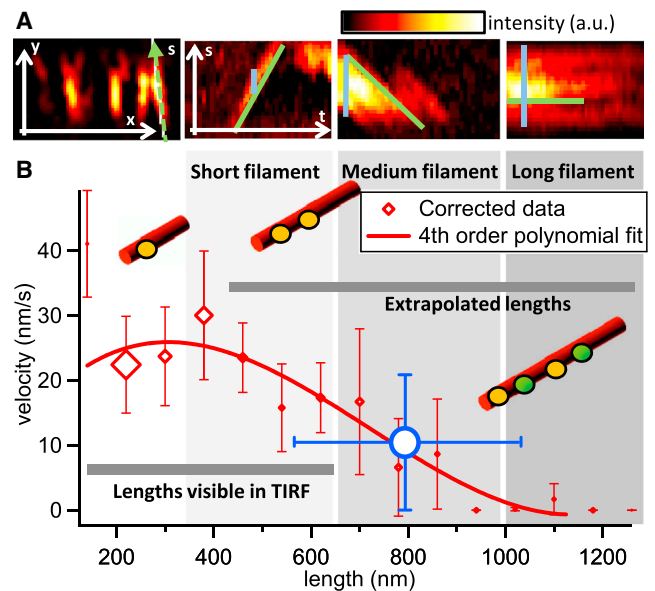


FIGURE 4 Dynamics of single MreB filaments. (A) Fluorescence image and kymographs of short, medium, and long filaments, where the slope of the filament edges (green line) indicates the velocity $v_F(L)$. The extent of the visible filament indicates the length L (blue line). (B) Mean filament velocities $\langle |v_F(L)| \rangle$ averaged over filaments of similar length L (bin size = 80 nm). $v_F(L)$ was measured by only one edge of each filament. For short filaments, $v_F(L)$ increases with length, whereas for longer filaments the velocity decreases linearly with an increasing number of acting (orange) and counteracting (green) motors (see sketched MreB filaments in red, with motors in orange and green). The red diamonds represent the velocities of both corrected and uncorrected filament lengths. Most filaments of length $L < 0.6 \mu\text{m}$ could be fully observed in TIRF-SIM. For $L = 0.4\text{--}1.3 \mu\text{m}$, lengths were corrected using the length distribution known from 3D-epifluorescence analysis (see Fig. S7 for details). The marker size corresponds to the number of filaments of similar lengths ($N_{total} = 105$), and the polynomial fit is of fourth order, $v_F = O(L^3)$. The round blue marker represents the mean velocity for all extrapolated lengths.

lengths of approximately $L = 0.35 \mu\text{m}$, a maximum transport velocity emerges. Fig. 4 B displays the observed velocities for a corrected length distribution. In TIRF-SIM, only velocities from filaments with lengths of up to 600 nm (both ends visible) can be measured. A length correction was applied to all filaments whose lengths were not completely visible in TIRF-SIM. Based on the TIRF-SIM observation that long filaments are slower or even rest, we extrapolated the unknown length for each measured velocity of a partly visible filament according to the length distribution known from 3D epifluorescence (for details, see Fig. S7). This provides a rough estimate about the velocity decay for longer filaments. The fourth-order polynomial fit serves as a guide to the eye and is the simplest and best fit to reflect the nonmonotonic behavior (see remark in Fig. S7). As we will discuss later in more detail, the putatively transporting motors operate cooperatively and thereby allow the filament velocity $v_F(L)$ to be regulated in such a way that both transport directions can occur and transport is slowed down for longer filaments.

DISCUSSION

Superresolution microscopy must be fast and minimize bleaching

Three principal imaging criteria must be fulfilled to achieve superresolved time series of dynamic MreB filaments. First, a sufficiently fast imaging technique is required to record the movements of filaments with velocities of up to 60 nm/s. Second, the total illumination energy deposited at the object must be kept as low as possible. This low photon dose allows one to acquire a sufficiently large number of images to achieve reasonable statistics for the MreB dynamics. Third, the optical resolution and the contrast must be so high that the filamentous structure of even short filaments can be revealed and cannot be misinterpreted as patches due to too much image blur (16,17). An ~120 nm spatial resolution inside the cell enabled us to identify several single-filament events of neighboring filaments, as presented in Fig. 2. In addition, the TIRF-SIM technique yields unequaled contrast because hardly any background fluorophores are excited. We determined that typically the acquisition of a superresolved image every 5 s is sufficient to track even fast filaments over a lateral bacterial cross section of $<1 \mu\text{m}$ (the diameter of the bacterium). The acquisition of one superresolved TIRF-SIM image requires nine sinusoidally modulated images, such that the overall energy deposit is 4.5 times higher than that for a single TIRF-image. Therefore, we could usually acquire a total of at least 30 images over $30 \times 5 \text{ s} = 2.5 \text{ min}$, which is hardly possible with any other superresolution imaging technique. Although superresolved 3D images using 3D-SIM would allow an even more unique and precise tracking of the filaments, an image stack consisting of at least seven planes (15 partial images per plane (28)) would significantly reduce the number of final images. Consequently, one could create ~10 times fewer points in time using 3D-SIM. Although STED microscopy offers a similar resolution (Fig. S8), fluorophore bleaching with commercially available systems is currently still too high to enable the required number of acquisitions. Techniques such as PALM/STORM are usually too slow to investigate MreB dynamics at an adequate signal/noise ratio and require special fluorophores. At the end of the image acquisition sequence, the cells had been exposed to a relatively high dose of fluorophore illumination energy, resulting in reactive oxygen radicals. Thus, we observed that stationary MreB filaments began to disassemble into shorter fragments.

A mechanistic model for MreB transport by coupled molecular motors

Although treadmilling has been reported to occur in *C. crescentus* cells (29), our measurements of single-filament transport (Fig. 2) reveal that a transport of MreB filaments by treadmilling is very unlikely in *B. subtilis*.

This is corroborated by observations in CW-less protoplasts, where MreB filaments remain stationary (Fig. S9 and Movie S4), and by the results of recent studies (16–18). Therefore, the other form of transport, i.e., biomolecular motors, which are universal in most eukaryotic cells, seems to be the putative driving mechanism for MreB filaments. More precisely, it has been hypothesized that PG monomers are added to the ends of PG strands by the enzymatic CW synthesis machinery, thereby driving the MreB filaments along the PG extension direction.

In the following text, we present a mechanistic model that is based on four simple assumptions and is able to explain all of the observed phenomena. First, it is reasonable to assume that the synthesis motors are uniformly distributed across the periphery of the cell, which does not exclude clustering of the motors to a certain extent. Second, we assume that longer filaments come into contact with more motors and shorter filaments contact fewer motors. Third, as the filaments are transported perpendicularly to the bacterial axis equally often in both directions, it is further evident that motors can act in both directions. In principle, this scenario can include plus- and minus-end-directed motors, as it is known for, e.g., myosin Va and VI proteins acting in opposite directions along polar actin filaments (30). However, for nonpolar filaments or an equal distribution of polar filaments oriented in both directions, a single motor type is sufficient. Hereafter, we will refer to plus-end (p) and minus-end (m) motors acting in the one or the other direction, respectively. Fourth, we assume that the motors bind and unbind stochastically via the transmembrane complex to MreB, as shown for the motions of different PBPs (16). Our model, which is based on exactly these four assumptions, is illustrated in Fig. 5 by a TIRF-SIM image of seven MreB filaments inside a cell and four corresponding sketches (Fig. 5, B–E). In Fig. 5 A, different measured lengths L are visible and different measured velocities v_F are indicated by white arrows. The scheme of Fig. 5 B depicts the corresponding model consisting of m- and p-polymerization motors (orange and green dots, respectively), which elongate blue PG strands and are connected to red MreB filaments. As displayed in Fig. 5 C and further discussed in the Supporting Material, text 2, one can estimate the angle β between the parallel PG strands and the MreB filament to be $\beta < \arcsin(\rho_M \cdot d_{PG}) \approx 5^\circ$, which is not measurable even with TIRF-SIM. Here, ρ_M is the motor density along the filament and d_{PG} is the distance between two neighboring PG strands. In the likely case that the on- and off-binding rates of the m-motors and p-motors are approximately equal, $k_{on,p} \approx k_{on,m}$ and $k_{off,p} \approx k_{off,m}$, the expected number of both motor types per filament should on average be equal. Obviously, it is more likely for longer filaments that the number of bound m-motors and p-motors will be roughly the same (i.e., that the ratio of m- and p-motors will be close to one) than for shorter filaments that bind to only a few motors.

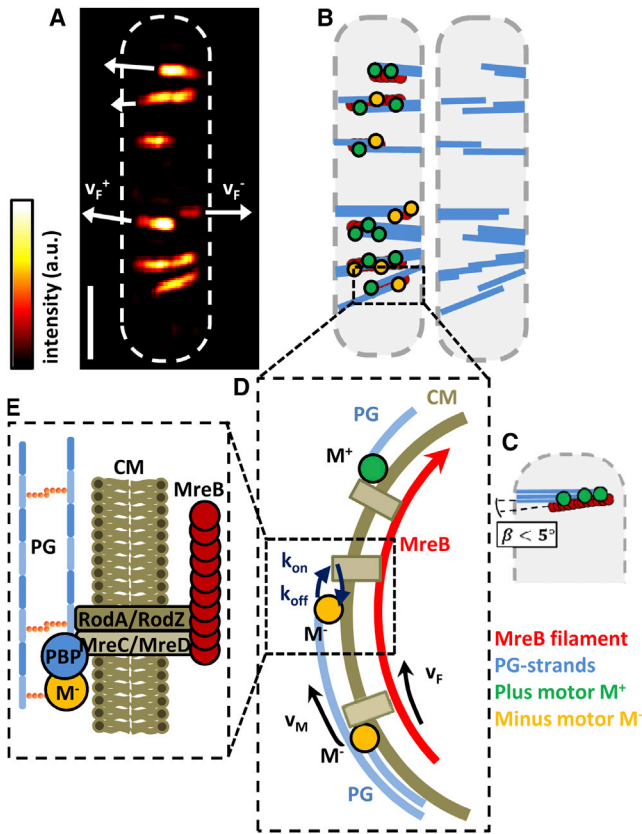


FIGURE 5 Schemes for MreB filament connection via membrane to motors as well as filament distribution. (A) TIRF-SIM image of MreB filaments and cell outline. Filament velocities (v_F^+ , v_F^-) are indicated by white arrows. Scale bar is $1 \mu\text{m}$. (B) Left: corresponding possible distribution of p- and m-motors, M^+ (green) and M^- (orange), as well as PG strands (blue). Resting filaments have an equal number of p- and m-motors attached. Right: the corresponding distribution of newly synthesized PG strands. (C) Scheme for an MreB filament organizing a concerted synthesis of three parallel PG strands by three synthesis motors. The angle $\beta < 5^\circ$ between the MreB filament and the PG strands cannot be resolved even with TIRF-SIM. (D) Motor movement enables filament transport with velocity v_F in either the p or m direction as long as at least one motor is bound with rate k_{on} via the transmembrane complex to MreB (k_{off} is the unbinding rate). (E) A motor M^- is bound to the PG strands and is connected via a protein complex (PBPs, RodA/RodZ, and MreC/MreD) through the CM to an MreB filament.

Based on our four simple assumptions, we can make the following conclusions: Because every motor type moves in its own direction, a tug-of-war is likely to occur, which would result in a blockade situation for an equal number of motors of both types. Filament transport in the p or m direction depends on whether the p-motors or m-motors win. For example, the larger the ratio of p-motors to m-motors, the more likely it is that the filament will be transported in the p direction. However, one can guess that the losing motors will not detach completely, but will try to rebind again, thereby hindering and slowing down the winning motors (31). An advanced tug-of-war model that considers the force-dependent unbinding rates of both motor types

has been computed and discussed extensively in the literature (32), especially in the context of myosin, kinesin, and dynein motors, and has found wide acceptance.

Monomer insertion rates and short filament velocities

Our mechanistic model is tested by the following observations and estimations: We observe a mainly smooth transport at a constant velocity without stopping over several acquisition time steps of $\delta t = 2\text{--}5 \text{ s}$, and thus can estimate a minimal (un-) binding rate of $k_{off/on} \gg 1/\delta t = (0.2\text{--}0.5) \text{ Hz}$. Furthermore, one may assume a mean value for a duty ratio of $R \approx 0.5\text{--}0.6$, which is close to values of R measured for processive myosin motors in eukaryotic cells (33). From $R = \tau_{on}/(\tau_{on} + \tau_{off}) = (1 + k_D)^{-1} \approx 0.5$, one can estimate a detachment constant $k_D = k_{off}/k_{on} \approx 1$, such that $k_{off} \approx k_{on}$. In the case of the PG synthesis motor, which inserts the PG monomers of approximate length $s_0 = 1 \text{ nm}$ (34) by hydrolyzing one ATP molecule, s_0 represents the motor's step size and $\bar{v}_M = v_M \times R = s_0 \times k_{ATP} \times R$ is its mean velocity. At our image acquisition rate, $1/\delta t$, we can measure only effective or mean filament velocities $\langle v_F \rangle$. However, for a short filament of $L \approx 0.15 \mu\text{m}$ (shown in Figs. 4 B and S7), we find a maximum filament velocity of $\langle v_F \rangle \approx v_M = 50 \text{ nm/s}$ and run length of approximately $\Delta x_M \geq 3 \times 5 \text{ s} \times v_M = 0.75 \mu\text{m}$ corresponding to the whole field of view that is observable by TIRF. One can guess that this filament was pulled by only one or two motors being constantly bound to MreB during the measurement time $\tau_{mes} \approx \tau_{on} \geq 3 \times 5 \text{ s} \gg (\tau_{on} + \tau_{off})$. From $v_M = s_0 \times k_{ATP} \approx 50 \text{ nm/s}$, one can estimate an insertion rate or ATP-hydrolysis rate of $k_{ATP} = 50 \text{ Hz}$. For the typical case in which $\tau_{mes} \gg (\tau_{on} + \tau_{off})$, the motor velocity drops down to $\bar{v}_M = v_M \times R = s_0 \times k_{ATP} \times R$. This estimate is simply to show that the parameters used are within a reasonable order of magnitude. Here, we assume that the transfer of the lipid II-PG precursor bond to the growing PG chain corresponds to the consumption of one ATP. The scenario is depicted in Fig. 5, D and E, where a p- or m-motor is connected via PBPs and a complex of RodA/RodZ/MreC/MreD to the MreB filaments. (The CW is synthesized through a putative large enzyme complex that contains proteins with transglycosylase and transpeptidase activities (e.g., PBPs). The depletion of PBPs and the membrane proteins MreC, MreD, and RodA leads to the formation of round cells, and PBPs, MreC, and MreD have been shown to physically interact with MreB. MreB consists of four transmembrane segments, whereas MreC has a small intracellular and a large extracellular domain, which is thought to mediate protein interactions. According to one model, MreB positions MreC and MreD, which in turn interact with and position PBPs, leading to a filament-organized CW synthesis (5)). However, as indicated by the rates k_{on} and k_{off} for on-binding and off-binding in Fig. 5 D, the

average transport velocity also depends on the time $\tau_{on} = 1/k_{off}$ the motors are bound.

Longer filaments move more slowly

According to our model and as outlined in Fig. 5 B, longer filaments are expected to be in contact with a larger number N of motors that move in either the p (green dots) or m direction (orange dots). The observed increase in velocity for filament lengths of up to $L = 350$ nm can be explained by the cooperative work of several motors, because the probability that at least one motor will bind and transport the filament is increased. However, since the mean filament velocity decreases after having reached a maximum, many motors must hinder each other. This slowdown is likely due to coacting motors obstructing each other's synthesis, as well as to counteracting motors that hinder the first type of motors during filament transport. In the putative case of a PG synthesis motor, it is difficult to imagine that these motors run backward, but rather detach from the filament. The unexpected slope of the curve $\langle v_F(L) \rangle$ revealing a maximum filament velocity (see Fig. 4) can be well expressed quantitatively by a multiple-motor model (31) as explained further below.

A reversal of the filament transport direction can be explained by our mechanistic model as follows: Especially short filaments tend to reverse their direction and change their angle of propagation (Movie S3). This observation is closely connected to the question as to what happens if a small, equal number of p- and m-motors start a tug-of-war. During the usually short tug-of-war, the short filament rests, but restarts to move at high velocity in one or the other direction as soon as the winning motor type has detached the losing motor type. If the counteracting motor type wins, the filament changes its direction. The longer the filament and the more synthesis motors are bound, the lower is the probability that significantly more motors of one type than of the other type will unbind at the same time, which could then result in a reversal of direction. As discussed in the following section, a change in the angular direction of transport is possible as well, since different motors are expected to move along different directions likely defined by the elongation of different PG strands. In other words, a direction reversal or reorientation of an MreB filament is connected to a stop of PG elongation in one direction and a start of PG elongation in another direction at the same location. However, the advantage of direction reversals for the CW's architecture remains unclear at this point.

Orientation of MreB filaments and PG strands

The following conclusion can be drawn from the data and our model: The filament transporting synthesis motors drive along parallel PG strands, which are expected to be in close proximity to each other, since otherwise the MreB filament

orientation would have a different angle compared with the trajectory (see Fig. 5 C). Because this is not visible, we estimate the lateral relative displacement between the motors to be equal to the lateral distance d_{PG} between two neighboring, cross-linked PG strands ($d_{PG} = 4$ nm) (36). Furthermore, the negligibly small tilt angle $\beta < \arcsin(\rho_M \cdot d_{PG}) \approx 5^\circ$ (Supporting Material, text 2) justifies the assumption that a temporarily unbound motor can quickly rebind to the MreB filament even if the latter was transported by other motors in the meantime. Therefore, we expect the synthesis velocity of several bound motors to be regulated by the filament velocity, because one motor cannot change its distance to the next one as long as several motors are bound. If a filament transported by N motors starts or stops, the synthesis of N parallel strands will be started or stopped. Because every motor activity is ATP powered and therefore rate limited, the motor displacement velocity is, generally speaking, controlled by a friction force produced by other motors coupled to the filament (31). This friction force, resulting from the coupling of MreB filaments to multiple PG strands, limits the synthesis velocity of single PG strands.

Mathematical model of the velocity-length-dependence

In the following, we will show that based on three of the four simple assumptions introduced above, we can quantitatively explain the nonmonotonic length-dependent velocity of MreB filaments with the simplest possible mathematical model. Our approach determines the mean number of bound motors to describe a cooperative motor transport as introduced by Klumpp and Lipowsky (31), and considers PG synthesis motors coacting in the same direction. The decelerating influence of counteracting motors is only implicit as part of a friction term Γ , as introduced further below. The filament velocity $v_F = v_F(L, R, \Gamma)$ depends on the number N of motors per filament and their attachment constant $k_{on}/k_{off} = R/(1-R)$ expressed by the duty ratio R . The filament length $L = N/\rho_M$ is assumed to be proportional to the number N of motors bound to it, divided by the as yet unknown mean motor density ρ_M . The shortest observable filament with a length of $L_{min} \approx 0.1 \mu\text{m}$ (optical resolution limit) was also among the fastest. Hence, an initial guess would be $\rho_M = 1/L_{min} = 10/\mu\text{m}$, assuming that the shortest filaments are transported by the least number of motors, which is $N = 1$. It should be emphasized that the motor density ρ_M could be higher than $10/\mu\text{m}$ without affecting the applicability of our model (Fig. S10). On the other hand, ρ_M cannot be much lower than $10/\mu\text{m}$, considering the proliferation time of the bacterium (Supporting Material, text 3).

In our mathematical model, the average filament velocity v_F would reach the single-motor velocity $v_M = s_0 \times k_{ATP}$ during the time when at least one motor is bound,

disregarding friction. The average binding time of a motor is determined by their attachment constant $R/(1-R)$. The longer the times in which no motor is bound, the more v_F is reduced (see two cases for $N = 4$ motors in Fig. 6 A). In addition, v_F is reduced by friction. The friction of the filament transport along the membrane, summarized by the dimensionless coefficient Γ , mainly results from the expected short attachments of counteracting motors and the mutual hindrance by coacting motors. In a first approximation, we assume the velocity reduction due to friction, $v_M \times \Gamma \times L \times \rho_M$, to be proportional to the filament length L or, equivalently, to the number of motors $N = L \times \rho_M$. The probability of finding exactly n out of N motors bound to a filament of length L can be expressed as $P_n(N, R) = P_0(N, R) \cdot (R/(1-R))^n$. Here $P_0(N, R) = 1/(\sum_{n=0}^N (R/(1-R))^n)$ describes the probability that no motor from the N motors is bound and serves as a normalization function, such that $\sum_{n=0}^N P_n(N, R) = 1$ (31). Therefore, the probability that at least one of the N motors will be bound is $\sum_{n=1}^N P_n(N, R) = 1 - P_0(N, R)$. Consequently, the length-dependent filament velocity can be expressed as

$$v_F(L, R, \Gamma) = k_{ATP} \cdot s_0 \cdot \left(\sum_{n=1}^{L \cdot \rho_M} P_n(L \cdot \rho_M, R) - \Gamma \cdot L \cdot \rho_M \right) \quad (1)$$

where $N = L \times \rho_M$. The length-dependent velocities predicted by this model are displayed in Fig. 6 for two different motor binding rates, k_{on} and k_{off} (duty ratios $R = 0.5$ and $R = 0.6$) with the value $\Gamma \approx 0.1$, which was chosen to fit to the measured data. According to Eq. 1, the model predicts that a short filament of the most frequently measured length $L \approx 0.2 \mu\text{m}$, driven by $N = 2$ motors is transported at an average velocity of $v_F(0.2\mu\text{m}, R, \Gamma = 0.1) = v_M \cdot (P_1(2, R) + P_2(2, R) - 0.1 \cdot 2) = 50 \text{ nm/s} \times (0.33 + 0.33 - 0.2) \approx 23 \text{ nm/s}$ (with $k_{ATP} = 50 \text{ Hz}$, $R = 0.5$, $\rho_M = 10/\mu\text{m}$). This velocity can be further increased due to the cooperative work of a few motors acting in the same direction (see further plots in Figs. S10 and S11). After reaching a maximum, the velocity v_F decreases approximately linearly with the filament length due to the total friction $N \times \Gamma \times v_M$, which increases linearly with the number of motors N . This observation is in agreement with the experimental results (see Fig. 6). For long filaments, v_F can become zero because many coacting and counteracting motors contribute to the deceleration. The smaller the duty ratio, the lower are the resulting velocities. This mathematical model cannot describe the observed reversals in direction of propagation because the action of counteracting motors is only incorporated in the friction coefficient Γ . Here, a more advanced tug-of-war model would describe the decreased velocity for longer filaments more realistically and could give further insights into the transport process (32).

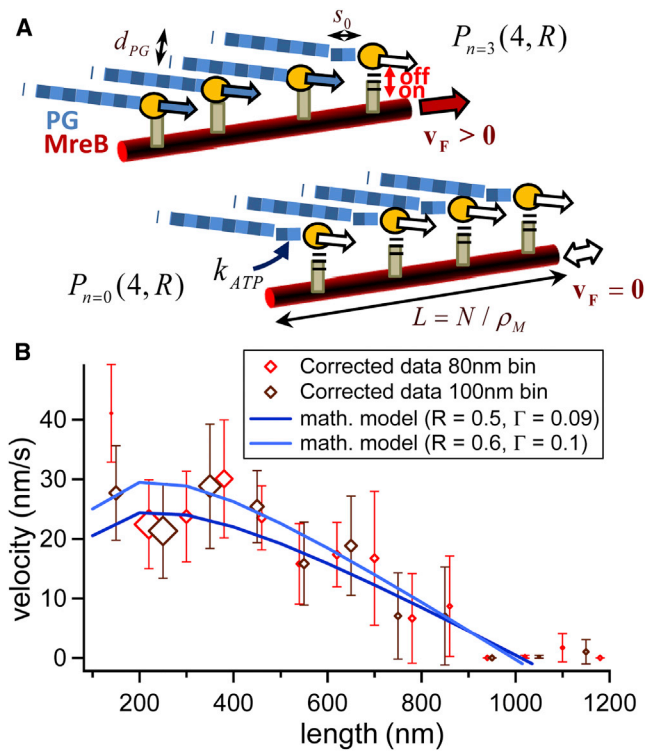


FIGURE 6 Mathematical modeling of length/velocity dependence. (A) Cartoon for two temporary binding states for a filament with $N = 4$ synthesis motors (orange dots) and of length $L = N/\rho_M$. Upper case: three of four motors are bound and transport the filament with $v_F = v_M = s_0 \times k_{ATP}$. Lower case: zero of four motors are bound and the filament stops for a very short time. In time average this filament's velocity would be $v_F = k_{ATP} \cdot s_0 \cdot (\sum_{n=1}^4 P_n(4, R) - \Gamma \cdot 4)$, according to Eq. (1). (B) Modeled and measured filament velocities as a function of filament length, which is proportional to the number N of motors. The stochastic model predicts an intermediate increase of the transport velocity due to the concerted action of the motors having duty ratios of $R = 0.5$ and $R = 0.6$ (light and dark blue, respectively). Each motor is decelerated by the same friction coefficient $\Gamma \approx 0.1$, leading to a linearly decreasing velocity for an increasing number of motors. The experimental data are plotted in light and dark red for two bin sizes and reveal the same nonlinear behavior.

MreB filaments organize the synthesis of the CW

We have demonstrated that MreB filaments move along straight trajectories that never cross each other. The connection of MreB via TMPs such as MreC and MreD to the CW constitutes a means of mechanical coupling between different regions on the periphery of the cell, as indicated in Fig. 5. The maximal coupling length is defined by the MreB length L , the coupling strength by both the bending rigidity and Young's tensile modulus of the filament and the linking TMPs. In the case of the PG synthesis machinery, a few strands would be synthesized in parallel at higher velocity, whereas a larger number of strands would be synthesized at lower velocity. If every synthesis motor were acting on its own, the disorder in the CW would increase and PG cross-linking might be reduced, resulting in a less stable CW.

According to our view, a change in transport direction (see Fig. 2, B and E) can occur when a majority of, e.g., p-motors is taken over by a majority of m-motors among all the motors that are interacting with the filament. This would require the insertion of PG monomers and peptide cross-linking of neighboring strands in opposite directions. According to the scheme of Fig. 5 D, the transmembrane complex RodA/RodZ/MreC/MreD would act as a direction-independent linker for motors driving in one or the other direction. As described in the Results, a reversal of direction can be induced when one MreB filament hits another, transport stops, and rebinding from one motor type to the other type is facilitated. However, some transport reversals apparently occurred spontaneously, either because one or several motors were stopped by opposing (invisible) PG strands or by a purely stochastic change of the motor type. It remains unclear why random transport reversals could be beneficial for the shape and stability of the cell.

If MreB is indeed driven by motors, it follows that its traces would reflect the motors' tracks. These tracks are straight and are likely to be the PG strands of the CW. Therefore, we think that the time projection of filament traces reflects those PG strands that have been newly synthesized during the observed time window. Because these traces never cross each other, one layer of the CW should consist of mainly parallel PG strands. From this, we conclude that the orientation of MreB filaments mirrors the orientation of group-wise parallel PG strands, as sketched in Fig. 5 B.

Finally, it should be stated that the multiple-motor model is nearly independent of the mean length of all filaments. It holds even for different expression levels of MreB, which may affect the filament lengths. The model works as well for bacteria being in the stationary phase, where MreB filaments become longer and slower, thereby reducing PG strand synthesis.

CONCLUSIONS

We have argued that among currently available technologies, TIRF-SIM seems to be the optimal imaging technique for studying MreB inside living bacteria, considering the spatial resolution, acquisition rate, and the total number of images due to moderate photobleaching. Using this technique, we could clearly show that similarly to actin, MreB forms filaments of different lengths rather than patches inside living *B. subtilis* cells. For filaments shorter than $\sim 0.35 \mu\text{m}$, the velocity of MreB filaments increases with length and can change direction within a few seconds. For longer filaments, transport velocities decrease with lengths. These dynamics can be explained by the cooperative work of several synthesis motors transporting MreB as cargos, which is similar to the collective behavior known for eukaryotic cells. Our mechanistic bidirectional, multimotor model is able to explain all of our observed data, which,

apart from the variable filament lengths, agree with observations from other groups (16–18). The allure of the model is that it only assumes that PG-synthesis motors are stochastically connected and disconnected to MreB, and that motors are equally distributed over the cell periphery. We have presented a mathematical simulation that is able to verify the unexpected velocity length dependence. Following these basic assumptions, MreB filaments can control the concerted synthesis of several PG strands across the periphery of the rod-shaped cell. The structure of the CW seems to be partly organized corresponding to the transport traces of MreB, whose filamentous form elongates several parallel PG strands. In summary, we believe that MreB serves as a mechanical coupler in organizing the bacterial CW by parallelizing PG strands both in synthesis velocity and in directionality, which is made possible by its filamentous structure.

SUPPORTING MATERIAL

Supporting information, 11 figures, four movies, and references (37–41) are available at [http://www.biophysj.org/biophysj/supplemental/S0006-3495\(13\)00860-6](http://www.biophysj.org/biophysj/supplemental/S0006-3495(13)00860-6).

The authors thank Prof. Roland Wedlich-Söldner, Dr. Stefan Klumpp, Felix Kohler, Jochen Stephan, and Jun.- Dr. Olaf Ronneberger for helpful discussions.

This study was supported by the Excellence Initiative of the German Federal and State Governments (EXC 294), and by grants SPP 1464 and FOR 929 from the Deutsche Forschungsgemeinschaft.

P.v.O. performed experiments, analyzed data, and prepared the graphs. P.G. and H.J.D.S. developed mutant lines and prepared the cells. R.H. and K.W. wrote the SIM reconstruction algorithms and helped with the image reconstruction. P.G. and A.R. initiated and supervised the project. A.R. and P.v.O. designed the microscopy system and developed the multimotor model. A.R. performed the mathematical modeling and wrote the manuscript together with P.G. and P.v.O.

REFERENCES

- Pollard, T. D. 2003. The cytoskeleton, cellular motility and the reductionist agenda. *Nature*. 422:741–745.
- van den Ent, F., L. A. Amos, and J. Löwe. 2001. Prokaryotic origin of the actin cytoskeleton. *Nature*. 413:39–44.
- Esue, O., M. Cordero, ..., Y. Tseng. 2005. The assembly of MreB, a prokaryotic homolog of actin. *J. Biol. Chem.* 280:2628–2635.
- Popp, D., A. Narita, ..., R. C. Robinson. 2010. Filament structure, organization, and dynamics in MreB sheets. *J. Biol. Chem.* 285:15858–15865.
- Graumann, P. L. 2007. Cytoskeletal elements in bacteria. *Annu. Rev. Microbiol.* 61:589–618.
- Defeu Soufo, H. J., and P. L. Graumann. 2006. Dynamic localization and interaction with other *Bacillus subtilis* actin-like proteins are important for the function of MreB. *Mol. Microbiol.* 62:1340–1356.
- Dye, N. A., Z. Pincus, ..., J. A. Theriot. 2011. Mutations in the nucleotide binding pocket of MreB can alter cell curvature and polar morphology in *Caulobacter*. *Mol. Microbiol.* 81:368–394.

8. Cowles, K. N., and Z. Gitai. 2010. Surface association and the MreB cytoskeleton regulate pilus production, localization and function in *Pseudomonas aeruginosa*. *Mol. Microbiol.* 76:1411–1426.
9. Defeu Soufo, H. J., and P. L. Graumann. 2005. *Bacillus subtilis* actin-like protein MreB influences the positioning of the replication machinery and requires membrane proteins MreC/D and other actin-like proteins for proper localization. *BMC Cell Biol.* 6:10.
10. Divakaruni, A. V., C. Baida, ..., J. W. Gober. 2007. The cell shape proteins MreB and MreC control cell morphogenesis by positioning cell wall synthetic complexes. *Mol. Microbiol.* 66:174–188.
11. Gitai, Z., N. Dye, and L. Shapiro. 2004. An actin-like gene can determine cell polarity in bacteria. *Proc. Natl. Acad. Sci. USA.* 101:8643–8648.
12. Varma, A., and K. D. Young. 2009. In *Escherichia coli*, MreB and FtsZ direct the synthesis of lateral cell wall via independent pathways that require PBP 2. *J. Bacteriol.* 191:3526–3533.
13. Figge, R. M., A. V. Divakaruni, and J. W. Gober. 2004. MreB, the cell shape-determining bacterial actin homologue, co-ordinates cell wall morphogenesis in *Caulobacter crescentus*. *Mol. Microbiol.* 51:1321–1332.
14. Scheffers, D. J., L. J. Jones, and J. Errington. 2004. Several distinct localization patterns for penicillin-binding proteins in *Bacillus subtilis*. *Mol. Microbiol.* 51:749–764.
15. Wang, S. Y., H. Arellano-Santoyo, ..., J. W. Shaevitz. 2010. Actin-like cytoskeleton filaments contribute to cell mechanics in bacteria. *Proc. Natl. Acad. Sci. USA.* 107:9182–9185.
16. Domínguez-Escobar, J., A. Chastanet, ..., R. Carballido-López. 2011. Processive movement of MreB-associated cell wall biosynthetic complexes in bacteria. *Science.* 333:225–228.
17. Garner, E. C., R. Bernard, ..., T. Mitchison. 2011. Coupled, circumferential motions of the cell wall synthesis machinery and MreB filaments in *B. subtilis*. *Science.* 333:222–225.
18. van Teeffelen, S., S. Wang, ..., Z. Gitai. 2011. The bacterial actin MreB rotates, and rotation depends on cell-wall assembly. *Proc. Natl. Acad. Sci. USA.* 108:15822–15827.
19. Eraso, J. M., and W. Margolin. 2011. Bacterial cell wall: thinking globally, actin locally. *Curr. Biol.* 21:R628–R630.
20. Hell, S. W., and J. Wichmann. 1994. Breaking the diffraction resolution limit by stimulated emission: stimulated-emission-depletion fluorescence microscopy. *Opt. Lett.* 19:780–782.
21. Betzig, E., G. H. Patterson, ..., H. F. Hess. 2006. Imaging intracellular fluorescent proteins at nanometer resolution. *Science.* 313:1642–1645.
22. Rust, M. J., M. Bates, and X. W. Zhuang. 2006. Sub-diffraction-limit imaging by stochastic optical reconstruction microscopy (STORM). *Nat. Methods.* 3:793–795.
23. Jones, S. A., S. H. Shim, ..., X. W. Zhuang. 2011. Fast, three-dimensional super-resolution imaging of live cells. *Nat. Methods.* 8:499–508.
24. Fiolka, R., M. Beck, and A. Stemmer. 2008. Structured illumination in total internal reflection fluorescence microscopy using a spatial light modulator. *Opt. Lett.* 33:1629–1631.
25. Defeu Soufo, H. J., and P. L. Graumann. 2004. Dynamic movement of actin-like proteins within bacterial cells. *EMBO Rep.* 5:789–794.
26. Kner, P., B. B. Chhun, ..., M. G. L. Gustafsson. 2009. Super-resolution video microscopy of live cells by structured illumination. *Nat. Methods.* 6:339–342.
27. Esue, O., D. Wirtz, and Y. Tseng. 2006. GTPase activity, structure, and mechanical properties of filaments assembled from bacterial cytoskeleton protein MreB. *J. Bacteriol.* 188:968–976.
28. Gustafsson, M. G. L., L. Shao, ..., J. W. Sedat. 2008. Three-dimensional resolution doubling in wide-field fluorescence microscopy by structured illumination. *Biophys. J.* 94:4957–4970.
29. Kim, S. Y., Z. Gitai, ..., W. E. Moerner. 2006. Single molecules of the bacterial actin MreB undergo directed treadmilling motion in *Caulobacter crescentus*. *Proc. Natl. Acad. Sci. USA.* 103:10929–10934.
30. Ali, M. Y., G. G. Kennedy, ..., D. M. Warshaw. 2011. Myosin Va and myosin VI coordinate their steps while engaged in an in vitro tug of war during cargo transport. *Proc. Natl. Acad. Sci. USA.* 108:E535–E541.
31. Klumpp, S., and R. Lipowsky. 2005. Cooperative cargo transport by several molecular motors. *Proc. Natl. Acad. Sci. USA.* 102:17284–17289.
32. Müller, M. J., S. Klumpp, and R. Lipowsky. 2008. Tug-of-war as a cooperative mechanism for bidirectional cargo transport by molecular motors. *Proc. Natl. Acad. Sci. USA.* 105:4609–4614.
33. Moore, J. R., E. B. Kremensova, ..., D. M. Warshaw. 2001. Myosin V exhibits a high duty cycle and large unitary displacement. *J. Cell Biol.* 155:625–635.
34. Carlstrom, D. 1957. The crystal structure of alpha-chitin (poly-N-acetyl-D-glucosamine). *J. Biophys. Biochem. Cytol.* 3:669–683.
35. Reference deleted in proof.
36. Vollmer, W., and J. V. Höltje. 2004. The architecture of the murein (peptidoglycan) in gram-negative bacteria: vertical scaffold or horizontal layer(s)? *J. Bacteriol.* 186:5978–5987.
37. Chang, S., and S. N. Cohen. 1979. High frequency transformation of *Bacillus subtilis* protoplasts by plasmid DNA. *Mol. Gen. Genet.* 168:111–115.
38. Hirvonen, L. M., K. Wicker, ..., R. Heintzmann. 2009. Structured illumination microscopy of a living cell. *Eur. Biophys. J.* 38:807–812.
39. Thévenaz, P., U. E. Ruttimann, and M. Unser. 1998. A pyramid approach to subpixel registration based on intensity. *IEEE Trans. Image Process.* 7:27–41.
40. Wicker, K., O. Mandula, ..., R. Heintzmann. 2013. Phase optimisation for structured illumination microscopy. *Opt. Express.* 21:2032–2049.
41. Löwe, J., F. van den Ent, and L. A. Amos. 2004. Molecules of the bacterial cytoskeleton. *Annu. Rev. Biophys. Biomol. Struct.* 33:177–198.